*h*BP-Fi: Contactless Blood Pressure Monitoring via Deep-Analyzed Hemodynamics

Yetong Cao* Shujie Zhang† Fan Li* Zhe Chen‡ Jun Luo†
* School of Computer Science and Technology, Beijing Institute of Technology, China
† School of Computer Science and Engineering, Nanyang Technological University, Singapore
‡ Intelligent Networking and Computing Research Center and School of Computer Science, Fudan University, China
Email: yetongcao@bit.edu.cn, shujie002@ntu.edu.sg, fli@bit.edu.cn, zhechen@fudan.edu.cn, junluo@ntu.edu.sg

***Abstract*—Blood pressure (BP) measurement is significant to the assessment of many dangerous health conditions. Apart from invasively inserting catheters into arteries, non-invasive approaches typically rely on wearing devices on specific skin areas with consistent pressure. However, this can be uncomfortable and unsuitable for certain individuals, and the accuracy of these methods may significantly decrease due to improper device placements and wearing states. Recently, contactless methods leveraging RF technology have emerged as a potential alternative. However, these methods suffer from the drawback of overfitting deep learning (DL) models without a sound *physiological* basis, resulting in a lack of clear explanations for their outputs. Consequently, such limitations lead to skepticism and distrust among medical experts. In this paper, we propose *h*BP-Fi, a contactless BP measurement system driven by *hemodynamics* acquired via RF sensing. In addition to its contactless convenience, *h*BP-Fi is superior to other RF sensing approaches in i) grounding on hemodynamics as the key physical process of heart-pulse activities, ii) exploiting beam-steerable RF devices to achieve a super-resolution scan on the fine-grained pulse activities along arm arteries, and iii) ensuring the trustworthiness of system outputs via an *explainable* (decision-understandable) DL model. Extensive experiments with 35 subjects demonstrate that *h*BP-Fi can achieve the error of -2.05±6.83 mmHg and 1.99±6.30 mmHg for monitoring systolic and diastolic blood pressures, respectively.**

I. Introduction

Hypertension, the leading risk factor for death, affects nearly half of the adults in the United States [1] and over 1.3 billion people globally [2]. As a silent condition that often develops over years without symptoms, it poses serious health risks such as heart attack, stroke, chronic heart failure, and kidney disease [1]. Therefore, regular monitoring of *blood pressure* (BP) is crucial for timely diagnosis [3]. Unlike serious hospital settings, regular BP measurements are normally non-invasive, obtained by strapping inflatable cuffs and sensors on arm [4], chest [5], wrist [6], [7], and ears [8], [9]. However, these methods require consistent application of pressure to specific skin areas, making them uncomfortable and unsuitable for individuals with sensitive or injured skin. Besides, the strict contact requirements limit their widespread adoption in daily life, particularly due to inaccuracies in BP measurements resulting from variable device placements and wearing states.

Fan Li is the corresponding author. This work is done when Yetong Cao works as a visiting scholar at NTU. The work of Fan Li is partially supported by the National Natural Science Foundation of China (NSFC) under Grant No. 62372045 and No. 62072040. The work of Zhe Chen is partially supported by NSFC under grant No. 62341105. The work of Jun Luo is partially supported by National Research Foundation (NRF) Future Communications Research & Development Programme (FCP) grant FCP-NTU-RG-2022-015.

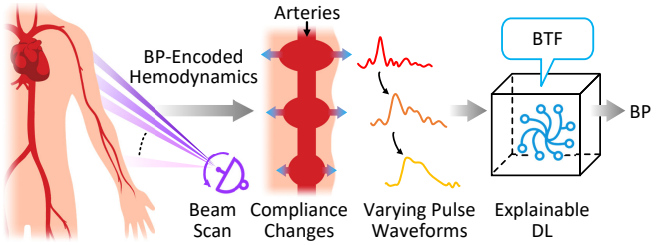

Fig. 1. The concept of *h*BP-Fi: a path from hemodynamics understanding towards RF (micro-)motion sensing and explainable DL inference.

Recent advancements in contactless sensing [10]–[14] bring new hope to alleviate these limitations, particularly through the use of *radio-frequency* (RF) sensing devices with wide bandwidth and high spatial resolution. Existing systems [15], [16] sense chest/arm motions as an externally observable biomarker and map the morphological features of the captured waveforms to BP via *deep learning* (DL). However, the learned mapping between morphological features and BP may not be causal due to the lack of a physiological basis. Moreover, DL models' failure to explain specific outputs has hindered their practical applicability in decision-sensitive medical contexts. Consequently, it is imperative to explore alternative approaches with sound physiological bases and enhanced explainability.

To this end, we present *h*BP-Fi to associate, for the first time, advanced RF sensing and DL inference with a sound physiological basis; it leverages motion-sensitive RF signals to capture the BP-encoded hemodynamics of pulses transiting along arm arteries. As shown in Fig. 1, as blood flows through, the arm arteries undergo compliance changes indicating changes in BP [19], resulting in variable pulse waveforms depending on the measurement site. Consequently, the varying pulse waveforms measured at different sites allow for deriving a *BP-specific transfer function* (BTF); inferring BP becomes possible as the BTF, describing how compliance varies along arteries, is causally related to BP. Specifically, *h*BP-Fi carefully steers RF beams to scan an arm, aiming to capture varying pulse waveforms along the arm. It then

TABLE I
COMPARISONS AMONG NON-INVASIVE BP MEASUREMENT METHODS, WITH THE ADVANTAGES OF *h*BP-FI HIGHLIGHTED.

Work	eBP [8]	Glabella [9]	Crisp-BP [6]	Fan *et al.* [17]	Ebrahim *et al.* [18]	mmBP [16]	*h*BP-Fi
Sensing modality	Oscillatory	PPG	PPG	Vision	RF	RF	RF
Non-physical contact	×	×	×	✓	×	✓	✓
Void of extra hardware	×	×	✓	✓	×	✓	✓
Output explainability	✓	×	×	×	×	×	✓
Physiological basis	✓	✓	✓	✓	×	×	✓
SBP mean/std (mmHg)	1.8/7.2	±10	1.67/7.31	8.42/8.81	<10	0.46/4.87	-2.05/6.83
DBP mean/std (mmHg)	-3.1/7.9	N/A	0.86/6.55	12.34/7.10	N/A	1.13/5.14	1.99/6.30

incorporates an explainable DL pipeline to derive the BTF that in turn leads to BP estimation in a decision-understandable manner. In Table I, we highlight the advantages of *h*BP-Fi over contemporary non-invasive BP measurement technologies.

Realizing this vision of *h*BP-Fi faces a few critical challenges. First of all, how RF signals respond to hemodynamics is unclear; one needs to build a solid physiological basis to connect them. Second, capturing high-quality pulse waveforms from multiple sites along an arm is crucial for accurate hemodynamics profiling. However, RF sensing devices such as mmWave radar [20] face limitations in pinpointing specific sites due to signal mixing from neighboring regions at the receiver, hindering direct support for hemodynamics profiling. Last but not least, the impact of time and temperature variations on BP estimation based on BTF highlights the need to employ DL technology for accurate monitoring in real-world environments. However, ensuring explainable decision-making processes to gain trust from medical applications is a less-explored research domain that lacks highly accurate solutions.

To address these challenges, we first carefully study the hemodynamics along arm arteries to figure out how the changes of RF-sensed pulse waveforms along the arm encode BP information. In particular, we characterize the relation between BP and varying pulse waveforms as a modified tube-load model [21]. We then specifically design a beam-steerable RF sensing scheme: though every single snapshot during this scanning process cannot focus on a particular site, our super-resolution scheme synthesizes all signals obtained during the whole scanning process to obtain a series of high-quality pulse waveforms along the arm. Finally, a DL pipeline is proposed to process pulse waveforms. Our innovative network construction and training with BTF constraints enable *h*BP-Fi to provide explanations for specific BP outputs, which ensures the reliability of the BP results. We highlight our main contributions as follows:

- Built up on a solid physiological basis, we propose *h*BP-Fi as the first contactless BP inference system leveraging explainable deep-analyzed hemodynamics.
- We thoroughly study the hemodynamics and reveal the intrinsic relation between arterial compliance and underlying BP variations. We introduce BTF to characterize this relation for the first time, with parameters specifically designed to be amenable to beam-steerable RF sensing.
- We propose a beam scan RF sensing scheme to obtain high-quality pulse waveforms along the arm; it performs super-resolution recovery of waveforms with a granularity finer than the minimum angular separation.
- We develop an explainable DL pipeline for BP inference, where the structure and searching space of loss function are constrained by BTF, ensuring explainability of the decision-making process and the reliability of the results.
- We thoroughly evaluated *h*BP-Fi via extensive experiments. The results demonstrate that *h*BP-Fi has an average error of -2.05±6.83 mmHg and 1.99±6.30 mmHg for *systolic blood pressure* (SBP) and *diastolic blood pressure* (DBP), respectively, which is within the acceptable range regulated by the FDA's AAMI protocol [22].

II. BACKGROUND AND MOTIVATIONS

A. Contact-based BP Measurement

While the gold standard BP is achieved by intravascular catheterization in an invasive manner, oscillometry-based solutions, primarily utilizing inflatable arm cuffs to compress the vessels, are commonly adopted due to their accessibility and noninvasiveness [4]. Nevertheless, cuff-based solutions pose certain limitations: i) the cuff's blockage of blood flow during measurement can cause discomfort, potentially resulting in tissue hypoxia, and are unsuitable for some individuals [23], ii) the performance is sensitive to cuff types and placements, making it challenging to achieve the desired accuracy in real-world scenarios. Despite efforts made by eBP [8] and HeartGuide [7] to mitigate discomfort through the integration of inflatable cuffs into earbuds and smartwatches, their performances remain sensitive to device-wearing states and placements, thereby impeding accurate BP monitoring.

With the advances in wearables and mobile devices, later efforts have leveraged easily accessible physiological signals acquired by these devices to infer BP. They are mainly based on the famous physiological fact that *pulse wave velocity* (PWV)

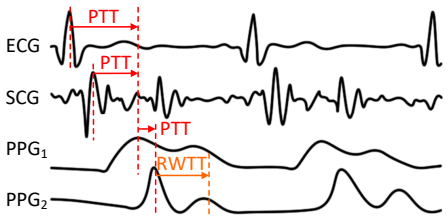

Fig. 2. Wearable sensors measure PTT and RWTT based on physiological signals from multiple sites. Curves are adapted from [5], [6], [9], [24].

is intrinsically related to BP variation [9], by $\text{PWV} = \ell/\text{PTT}$ where PTT refers to the *pulse transit time*, the traveling time of pulse waves between two arterial sites, and ℓ denotes the distance in-between; here *pulse* is a shortened form of *blood volume pulse*. This actually converts BP measurements to BP inference via PTT measurements. Fig. 2 shows examples of measuring PTT from peak delay between two physiological signal pairs, such as ECG-PPG [5], SCG-PPG [24], and PPG-PPG [9]. However, these approaches are both inconvenient and unreliable, because they need to attach multiple wearable sensors to a body and their performances are highly dependent on sensor placements: tiny changes on the sites of any sensors can cause dramatic performance degradation [16]. Recently, Crisp-BP [6] exploits *reflected wave transit time* (RWTT) readily obtainable by a wrist PPG sensor to replace PTT for inferring BP, yet it is still sensitive to wearing states due to its wearable nature.

B. How About Contactless Solutions?

Given the drawbacks of contact-based solutions, such as inconvenience, discomfort for some individuals, and sensitivity to device-wearing states and placements, it is natural to consider resorting to contactless solutions. We first briefly discuss a few typical attempts, and then turn our focus to studying the major obstacle preventing them from getting practical.

1) Why Existing Contactless Fails: Early attempts centered on using cameras to deduce PTT from remote-PPG and in turn infer BP [17], [25], [26]. However, camera-based solutions require strict recording conditions, such as adequate lighting and the entire view of a face. Besides, the incurred privacy concerns further limit their wide adoption. Subsequently, RF-sensing is employed in combination with wearable ECG or PPG sensors to obtain PTT and infer BP [18], [27], leveraging the advantages of less strict recording conditions and mitigating privacy concerns. However, precisely synchronizing these sensors (of very different modalities) can be extremely challenging. Moreover, coarse-grained RF sensing fails to isolate specific measurement sites and instead captures mixed signals from neighboring regions [16]. This limitation results in inaccurate BP estimations when applying the site-sensitive PTT-based solution, as demonstrated in Sec. II-B2).

Given the challenges encountered by the above approaches, recent RF-based contactless BP solutions have resorted to a *black box* DL pipeline [15], [16]. These solutions utilize RF sensing to extract pulse activities as a biomarker and employ DL models to map their morphological features to BP in a brute-force manner. While they report impressive BP accuracy, the non-causal mapping between morphological features and certain BP values lacks a physiological basis, raising concerns about their reliability and the potential for biased BP estimates resulting from DL overfitting. Moreover, the lack of explainability in *black box* DL models impedes the adoption of these systems in decision-sensitive healthcare scenarios, as it hinders the understanding of how and why certain BP values are determined, consequently further undermining the trustworthiness of BP estimates.

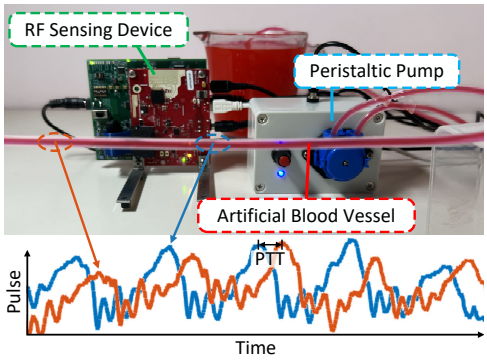

Fig. 3. In-vitro blood circulation simulator to study PTT measured by RF sensing technology.

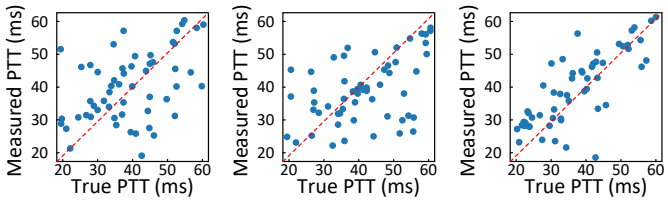

(a) 4 Tx-Rx pairs (b) 6 Tx-Rx pairs (c) 8 Tx-Rx pairs

Fig. 4. Comparing measured PTTs with true PTTs for different Tx-Rx pairs.

2) Acquiring Pulse Activities by Scan: Recent advances in RF sensing have equipped devices (e.g., mmWave radar) with antenna arrays; they allow RF radiation beams to be steered towards certain directions. A natural yet novel idea would be leveraging the beam-steerable RF sensing to extract pulses waveforms from two specific directions using the same device to derive PTT: This is superior to existing PTT-enabled RF sensing proposals that require extra sensing modalities and cumbersome synchronization among these distinct modalities.

We build a blood circulation simulator as shown in Fig. 3; it uses a peristaltic pump [28] to emulate how blood flows through blood vessels at different PWVs. [1] An mmWave radar [20] is adopted to perform beam-steerable sensing. We in particular pick two measurement sites and measure the time delay between the pulse waveforms extracted from these two sites (elaborations on how to obtain pulse waveforms are given in Sec. III-B2). The true PTT is computed as the ratio of the distance between the measurement sites and the known PWV specified by the pump. Fig. 4 compares the measured PTTs with the true ones under 4, 6, and 8 antenna pairs. Although the results do not appear to be perfect, more antenna pairs evidently yield better results, because the angle resolution of the radar is determined by the number of transmitting antenna (Tx) and receiving antenna (Rx) pairs. Nonetheless, the estimation error is still excessive even with 8 Tx-Rx pairs, *indicating a deficit of such a straightforward usage of beam-steerable sensing.* Motivated by the above observations, we set out to establish a new mathematical model that reveals the link between pulse activities and BP in Sec. III-A, and to design an effective beam-steerable sensing scheme for achieving super-resolution extraction of pulse waveforms in Sec. III-B.

[1] We adjust the PWVs within the normal PWV range of [3,9] m/s [29].

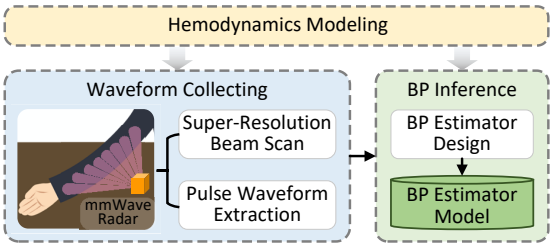

Fig. 5. System architecture of *h*BP-Fi.

III. System Design

As illustrated in Fig. 5, *h*BP-Fi is mainly composed of three components: *Hemodynamics Modeling*, *Waveform Collecting*, and *BP Inference*. Since vascular compliance (elastic modulus) is affected by BP, *Hemodynamics Modeling* aims to associate the pulse activity captured by RF sensing with the implicit compliance property. To this end, a tube-load model is adopted to describe the hemodynamics, which leads to a novel mapping, BTF, that relates changes in compliance to those in the pulse waveforms propagating through different measurement sites. With this theoretical basis, *h*BP-Fi leverages an mmWave radar in *Waveform Collecting* to achieve adequate resolution for pulse activity sensing by extracting pulse waveforms out of phase changes in RF reflections along the arm. Finally, *BP Inference* inputs BTFs measured from the *Waveform Collecting* to an explainable DL pipeline based on the DRCN to reliably infer BP. In particular, the system incorporates innovative design in the model's structure and the searching space of the loss function, enabling users to understand and interpret the decision-making process of the DL model in deriving certain BP measurements. For the actual measurement (also shown in Fig. 5), we require the subject to i) stretch his/her arm on a table, ii) maintain minimal body movement, iii) keep a fixed distance (e.g., 50cm) from the radar (on the same table) whose field of view (FoV) sufficiently covers the whole arm.

A. Hemodynamics Modeling via BTF

Hemodynamics refers to the process of how blood flows through the blood vessels. As the heart beats, it pumps blood through the circulatory system formed by blood vessels, generating pressure to push the elastic vessel wall outwards, which is then bounced back after the blood passes through. Among all physiological indicators of hemodynamics, BP indicates the radial pressure caused by the blood flow, whose continuous representation is pulse activities.

Herein, we explain the hemodynamics based on the widely recognized tube-load model [21] with additional accounting for BP-dependent arterial compliance and peripheral wave reflection [19]. As shown in Fig. 6(a), the blood vessel is modeled as a single uniform frictionless tube that has BP-related characteristic impedance of $Z_c = \sqrt{\eta/C(\rho)}$ to support blood travel from the start to the end, where η is the constant inertance of the tube, $C(\rho)$ is the BP-related compliance (elastic modulus) of the tube, and ρ represents the BP. According to the Young's modulus, the relationship between compliance

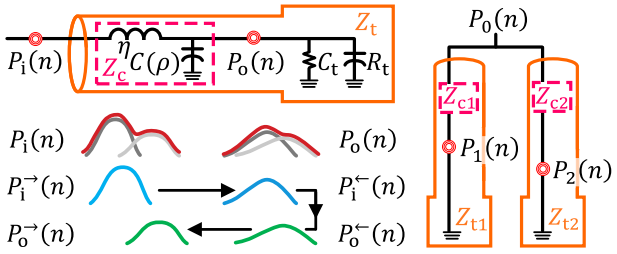

(a) The tube-load model of blood vessel. (b) An instance.

Fig. 6. Hemodynamics modeling (a) and an instance of modeling BTF at different sites (b).

of the elastic tube and the distending pressure ρ is described by the expression [19]:

$$C(\rho) = C_0 e^{-\alpha\rho}, \tag{1}$$

where α is the vessel parameter and C_0 is Young's modulus for zero arterial pressure. Their values are constant and subject-specific, as widely validated by existing studies [30]. Besides, the peripheral vessels are modeled as the three-element Windkessel terminal load [31], which has an impedance Z_t determined by i) characteristic impedance Z_c, ii) peripheral resistance exerted by the arterioles R_t, and iii) compliance of the distal arteries C_t, via $Z_t = Z_c + R_t/(1 + R_t C_t)$.

We denote the pulse waves at the tube *inlet* in time t as $P_i(t)$ and those at the tube *outlet* as $P_o(t)$. They consist of forward and backward waves, both traveling with delay and distortion characterized by a wave propagation function $\phi(\rho)$ via $P_o^{\rightarrow}(t) = e^{\phi(\rho)\ell} P_i^{\rightarrow}(t)$ and $P_i^{\leftarrow}(t) = e^{\phi(\rho)\ell} P_o^{\leftarrow}(t)$ [21], where the superscripts $\rightarrow$ and $\leftarrow$ represent the forward and backward components, respectively, and ℓ is the length of the tube. Moreover, the backward waves are generated by the forward ones encountering a change in impedance at the terminal load, leading to the following relation:

$$P_o^{\leftarrow}(t) = \Psi P_o^{\rightarrow}(t) = \frac{as}{s^2 + bs} P_o^{\rightarrow}(t), \tag{2}$$

where s is the Laplace variable, $a = 1/2Z_cC_t$, and $b = a + 1/R_tC_t$. Using Eqn. (2) and based on that $P_o(t)$ and $P_i(t)$ are the sum of forward and backward waves, the relation between $P_o(t)$ and $P_i(t)$ can be modeled by a *BP-specific transfer function* (BTF) $\Gamma_{i\to o}$ as:

$$P_o(t) = \Gamma_{i\to o} P_i(t) = \frac{1 + \Psi}{e^{\phi(\rho)\ell} + e^{-\phi(\rho)\ell}\Psi} P_i(t). \tag{3}$$

Considering that the tube is frictionless, $\phi(\rho)$ can be reduced to $\sqrt{\eta C(\rho)}$ via the Taylor series expansion. Altogether, the BTF can be presented as:

$$\Gamma_{i\to o} = \frac{s^2 + (b+a)s}{(s^2 + bs)e^{\ell\sqrt{\eta C(\rho)}} + ase^{-\ell\sqrt{\eta C(\rho)}}}, \tag{4}$$

where polynomial coefficients a, b, and constants related to $C(\rho)$ (i.e., η, C_0, α) can be readily determined by population-based normative values or subject-specific least-squares formulation. Finally, we conclude that the BTF is the function of only ℓ and ρ. Ideally, given observed $P_o(t)$ and $P_i(t)$,

one can first measure the BTF via $\Gamma_{\mathrm{i}\to\mathrm{o}} = P_{\mathrm{o}}(t)P_{\mathrm{i}}^{-1}(t)$. Then the BP value ρ can be determined by Eqn. (4) in the least-squares sense, with prior knowledge of the precise artery length between the two sites, i.e., ℓ. It is worth noting that the above relation still holds when $P_{\mathrm{i}}(t)$ and $P_{\mathrm{o}}(t)$ are superimposed by multiple pulses, which is equivalent to the parallel connection of multiple tubes with loads [32].

In practice, precise measurement of ℓ is the major obstacle to solving BTF and thus inferring BP. Instead of dwelling on perfecting the estimation of ℓ, we relate BP and BTF via optimization. We first consider three pulse waveforms measured at different locations, as shown in Fig. 6(b), denoted by $P_0(t)$, $P_1(t)$, and $P_2(t)$. According to Eqn.(3), we have $P_1(t) = \Gamma_{0\to1}(\Theta)P_0(t)$ and $P_2(t) = \Gamma_{0\to2}(\Theta)P_0(t)$, where $\Theta \triangleq \{\rho, \ell_{0\to1}, \ell_{0\to2}\}$ defines the parameter set. Since $\Gamma_{0\to1}(\Theta)^{-1}P_1(t) = P_0(t) = \Gamma_{0\to2}^{-1}P_2(t)$, we tune the parameters of Θ by minimizing the following:

$$\min_{\Theta} J(\Theta) = \min_{\Theta} \left\| \Gamma_{0\to2}(\Theta)^{-1}P_2(t) - \Gamma_{0\to1}(\Theta)^{-1}P_1(t) \right\|_2. \quad (5)$$

Several mathematical relations can be incorporated to narrow the searching space for the optimal Θ. Under our context, RF sensing may help infer the radial range and bearing between the RF device and the measurement sites, which in turn leads to estimations of $\ell_{0\to1}$, $\ell_{0\to2}$, and $\ell_{1\to2}$ via trigonometry operations. More importantly, Eqn. (5) can be extended to accommodate an arbitrary number n of pulse waveforms measured at different locations, further helping constrain the parameter set $\Theta \triangleq \{\rho, \ell_{0\to1}, \ell_{0\to2}, ..., \ell_{0\to n}\}$ and potentially yielding a more accurate estimation to BP ρ. In the following, we shall design *h*BP-Fi to capture fine-grained pulse waveforms from as many well-distinguishable skin sites as possible, so as to achieve accurate BP inference.

B. RF Pulse Waveform Collection

*h*BP-Fi employs steerable RF beams to scan the skin vibrations induced by pulse along human arm. Particularly, steerable beam patterns are employed in a time-division manner, enabling the RF beam to scan successive directions with a μs-level delay to capture spatially separated pulse waveforms along an arm. In the following, we first discuss how to achieve a super-resolution beam scan, then we elaborate on the waveform extraction scheme.

1) Super-Resolution Beam Scan: RF signals transmitted and received by mmWave radars (with MIMO antennas) are often directional, achieved by beamforming at both transmitter (Tx) and receiver (Rx) sides. Whereas existing RF human sensing technologies mostly place a subject at zero-degree bearing to ensure sufficient signal quality, our analysis in Sec. III-A shows that capturing pulse waveforms at different arm sites with beam scan is possible, but the angle-resolution achieved by the default beamforming scheme is highly inadequate. Therefore, we need to substantially improve the angle-resolution for *h*BP-Fi.

We consider a uniform linear array (ULA) with N Tx antennas spaced by d_{tx} and M Rx antennas spaced by d_{rx}.

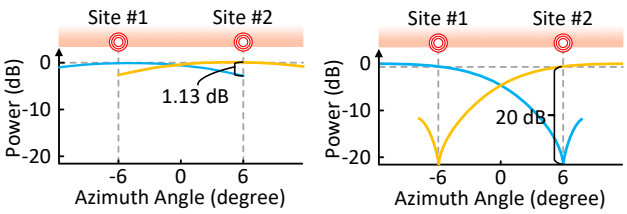

(a) Main beams. (b) Null point beams.

Fig. 7. Comparing beam patterns for two neighboring arm sites of an angular separation smaller than the width of the main beam.

To scan multiple sites, we program the Tx antennas to successively steer the beam towards different directions in a time-division manner, by emitting RF signals with distinct phase combinations in each time slot. During the k-th time slot, to focus the signals towards a bearing θ, the phase combination for Tx antennas is determined as:

$$\vec{\phi}(\theta) = [0, \frac{2\pi d_{\mathrm{tx}} \sin\theta}{\lambda}, ..., (N-1)\frac{2\pi d_{\mathrm{tx}} \sin\theta}{\lambda}], \quad (6)$$

where λ is the signal wavelength; this endows directionality to the RF sensing.

However, it is highly non-trivial to separate the RF reflections from different arm sites: the limited antennas along with short distance between arm and radar force the reflected signals from main (or even side) beams to get merged together, rendering the boundaries between neighboring sites very vague. For simplicity, we use two main beams to demonstrate the worst case phenomenon of the merged signals for sensing pulse from two neighboring arm sites in Fig. 12(a). Assuming a ULA with 8 Tx-Rx pairs whose beamwidth is approximately 14°, pulse waveforms from sites #1 and #2 separated by 12° are indistinguishable as the magnitude difference between two main beams is only 1.13 dB [33]. Such a phenomenon makes the default radar beamforming scheme insufficient to obtain fine-grained pulse waveforms for deriving accurate BTFs needed by Eqn. (5). Therefore, we should consider exploring a new method to separate the RF reflections from neighboring arm sites.

To magnify the difference of the RF reflections from two neighboring sites with an angular separation smaller than the width of the main beam, we propose a *differential beamforming with null-steering* scheme to achieve super-resolution beam scan. Null-steering is originally proposed to reject unwanted interference sources arriving from a known direction by producing a null point in the response pattern [34]. As shown in Fig. 12(b), in the case of using a ULA with 8 Tx-Rx pairs, two beams whose null points are separated by 12° yield a remarkable 20 dB amplitude differences between the two main beams, rendering pulse waveforms at the two sites highly distinguishable.

Herein, we present our null-steering via an example of separating RF signals from two sites denoted by $\Phi_1(t)$ and $\Phi_2(t)$, respectively. The RF signals received in a time slot can be expressed as [35]:

$$\mathbf{y}_p(t) = \mathbf{v}(\theta_1)\Phi_1(t) + \mathbf{v}(\theta_2)\Phi_2(t), \quad (7)$$

where $\mathbf{v}(\theta) = [1, e^{j\alpha(\theta)}, ..., e^{j(M-1)\alpha(\theta)}]$ is the Rx direction vector with $\alpha(\theta) = \frac{2\pi d_{\mathrm{rx}} \sin\theta}{\lambda}$.

By assigning differential weights to the received signals, one can formulate the following:

$$\begin{aligned} s_1(t) &= \mathbf{w}_1^H \mathbf{y}_p(t) = [1, e^{j\alpha(\theta_1)-\vartheta}, ..., e^{j(M-1)\alpha(\theta_1)-\vartheta}]^\top \mathbf{y}_p(t) \\ s_2(t) &= \mathbf{w}_2^H \mathbf{y}_p(t) = [1, e^{j\alpha(\theta_1)+\vartheta}, ..., e^{j(M-1)\alpha(\theta_1)+\vartheta}]^\top \mathbf{y}_p(t) \end{aligned}, \quad (8)$$

where $\vartheta = \pi/180$ is a small constant and θ_1 indicates the null point. Associating Eqn. (7)-(8), we have

$$s_1(t) = a_{11}\Phi_1(t) + a_{12}\Phi_2(t) \quad s_2(t) = a_{21}\Phi_1(t) + a_{22}\Phi_2(t),$$

where $\Delta\theta = 2\pi d_{\text{rx}}(\sin\theta_2 - \sin\theta_1)/\lambda$ and $\{a_{11}, a_{12}, a_{21}, a_{22}\}$= $\left\{\sum_{m=0}^{M-1} e^{j\vartheta m}, \sum_{m=0}^{M-1} e^{j(\Delta\theta+\vartheta)m}, \sum_{m=0}^{M-1} e^{-j\vartheta m}, \sum_{m=0}^{M-1} e^{j(\Delta\theta-\vartheta)m}\right\}$.

According to the Euler's formula, the complex amplitude a_{11} can be rewritten via

$$\begin{aligned} a_{11} &= e^{j\frac{M-1}{2}\vartheta}(e^{-j\frac{M-1}{2}\vartheta} + e^{-j\frac{M-3}{2}\vartheta} .... + e^{j\frac{M-3}{2}\vartheta} + e^{j\frac{M-1}{2}\vartheta}) \\ &= e^{j\frac{M-1}{2}\vartheta}(2\cos\frac{(M-1)\vartheta}{2} + 2\cos\frac{(M-3)\vartheta}{2} + ...). \end{aligned} \quad (9)$$

Applying the same derivation method, the remaining complex amplitudes can be expressed by the following:

$$\begin{aligned} a_{12} &= e^{-j\frac{M-1}{2}(\Delta\theta+\vartheta)}(2\cos((\Delta\theta+\vartheta)(M-1)/2) \\ &\quad + 2\cos((\Delta\theta+\vartheta)(M-3)/2) + ...), \\ a_{21} &= e^{-j\frac{M-1}{2}\vartheta}(2\cos\frac{(M-1)\vartheta}{2} + 2\cos\frac{(M-3)\vartheta}{2} + ...), \\ a_{22} &= e^{-j\frac{M-1}{2}(\Delta\theta-\vartheta)}(2\cos((\Delta\theta+\vartheta)(M-1)/2) \\ &\quad + 2\cos((\Delta\theta-\vartheta)(M-3)/2) + ...). \end{aligned} \quad (10)$$

Since a_{11} and a_{21} have the same amplitude but only differ in phase, we can extract $\Phi_2(t)$ by calibrating the phase difference and subtracting the calibrated signals:

$$\begin{aligned} \delta s(t) &= s_2(t)e^{j\frac{M-1}{2}\vartheta} - s_1 e^{-j\frac{M-1}{2}\vartheta} \\ &= \Phi_2(t)e^{j\frac{M-1}{2}\Delta\theta}(4\sin\frac{(M-1)\Delta\theta}{2}\sin\frac{(M-1)\vartheta}{2} \\ &\quad + 4\sin\frac{(M-3)\Delta\theta}{2}\sin\frac{(M-3)\vartheta}{2} + ...). \end{aligned} \quad (11)$$

Using the same method, $\Phi_1(t)$ can be readily obtained by replacing the null point in Eqn. (8) from θ_1 to θ_2.

2) Pulse Waveform Extraction: The mmWave radar in *h*BP-Fi utilizes an FMCW waveform, a sine wave with a linearly increasing frequency over time [14]. Skin vibrations induced by pulses cause minor distance variations that modulate the reflected FMCW signals and affect their phase. Rx antennas collect these reflections, and IF signals (differential signal between Tx and Rx chirps) are processed by range FFT to determine arm distance [36]. This is followed by the differential beamforming with null-steering to further separate the data from different arm sites. After processing multiple chirps, the reflections from each arm site form a complex radar data tensor $X(d, q, v)$, where d, q, and v represent distance bin, chirps, and arm sites, respectively. Leveraging the real and imaginary components of $X(d, q, v)$, the phase variations $\Delta\phi$ incurred by pulse activities can be readily obtained.

We recruit four subjects and apply the aforementioned method to measure their pulses in real-world environments for three months. Examples of pulse waveforms from two arm sites, separated by a 12° angle, are shown in Fig. 8(a)-8(d), with different colors representing distinct sites, confirming the successful resolution enhancement of our method. Then, we estimate BP based on these collected pulse waveforms as described in Sec. III-A. Fig. 8(e)- 8(f) compares the estimated BP results and true BP, using different colors to distinguish users. The figures clearly demonstrate a strong correlation (correlation coefficient > 0.8) between the estimated and true BP, further confirming the feasibility of employing the BTF model for BP inference. Notably, the errors between the estimated and true BP occasionally exceed medical standards, attributed to the influence of temperature and time of day in real-world environments, which the current BTF model fails to address. This insight inspires us to utilize the power of DL techniques to attain more precise BP results.

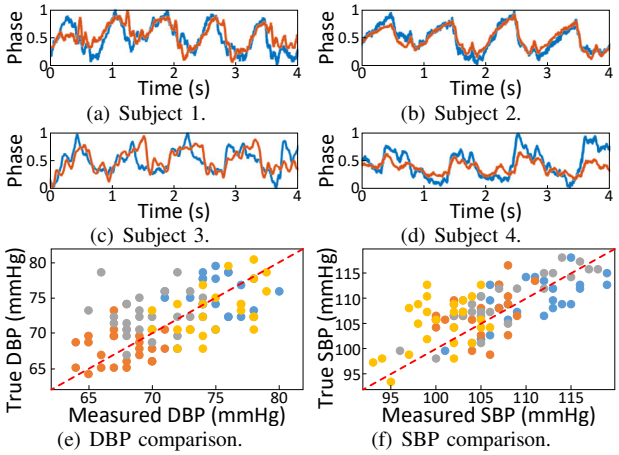

Fig. 8. Examples of pulse waveforms obtained from four subjects (a-d), and comparisons between BP inferred via BTF and true BP (e-f).

C. BP Inference

To address the limitations of directly using the mathematical BTF model (lack of adaptability to environment factors), we integrate BTF with a DL framework to overcome the challenge of *black box* DL.

The combination of mathematical model and DL have proven effective in various tasks [37], often achieved through a cascading approach: using a rough mathematical model for initialization and refining the results with DL, or using DL to extract features as prior information for an accurate mathematical model. However, these solutions require manual parameter adjustments and only provide shallow feature priors [38]. To overcome these limitations, we propose a novel DL framework with a structure specifically designed based on the BTF model, constraining the search space of the loss function accordingly. This allows the users and medical experts to gain understanding of how and why specific BP outcomes are obtained from the inputted BTFs, thereby facilitating the acceptance and application of *h*BP-Fi in decision-sensitive medical services.

Particularly, we build *h*BP-Fi's BP estimator upon deeply-recursive convolutional network (DRCN) to optimize the BTF model parameters, which is followed by long short-term memory (LSTM) modules to obtain the BP estimates. Specifically, BTFs are first measured from the time series of varying pulse waveforms via $\Gamma_{\text{i}\to\text{o}} = P_{\text{o}}(t)P_{\text{i}}^{-1}(t)$. As shown in Fig. 9,

the BP estimator takes the measured BTFs as input, then it splits the optimization of Eqn. (5) into sub-problems based on alternating direction method of multipliers [39] as follows:

$$\begin{aligned}\Theta^{t+1} &= \Theta^t - \eta\frac{\partial}{\partial\Theta^t}J(\Theta) + \frac{\gamma}{2}\left\|\lambda^t + A\Theta^t + BZ^t - C\right\|_2^2 \\ Z^{t+1} &= \mathbf{DRCN}(\Theta^{t+1}, \lambda^t) \\ \lambda^{t+1} &= \lambda^t + A\Theta^{t+1} + BZ^{t+1} - C\end{aligned}, \quad (12)$$

which is subject to $A\Theta + BZ = C$, and λ is the Lagrange multiplier, γ is the penalty parameter. Each iteration is unfolded into one sub-network in recursion, which forms multi-cascaded sub-networks sharing the same network parameters. The BTF-constrained DRCN is the core of combining the BTF model with DL, which automates the iterative optimization and variable splitting (commonly used in model-driven optimization) through DL, making the proposed DL framework explainable. The follow-up LSTM modules utilize the latent BP information from the optimized DRCN model to mitigate environmental variations, ultimately fine-tuning the SBP and DBP results through dense neuron layers.

The loss function for estimation commonly adopts the mean square error (MSE) to minimize the difference between the network output and the ground truth values, which potentially causes biased BP estimates due to potential DL overfitting. As *h*BP-Fi is concretely based on hemodynamics, we additionally take into account the error of the BTF optimization to establish the BTF-constrained loss function:

$$\mathfrak{L}(E_\rho) = \|J(\Theta)\|_2^2 + \|A\Theta + BZ - C\|_F^2 + \|\rho - \tilde{\rho}\|_2^2, \quad (13)$$

where $\|\cdot\|_F$ represents the Frobenius norm, $\rho = \{\rho_\mathrm{s}, \rho_\mathrm{d}\}$ and $\tilde{\rho} = \{\tilde{\rho}_\mathrm{s}, \tilde{\rho}_\mathrm{d}\}$ denote the ground truth values and estimated values of SBP and DBP, respectively. This loss function takes the BTF-constrained parameter optimization as a regularization term, rendering the optimization space explainable. Overall, the explainable structure and explainable optimization spaces render the decision-making processes explainable, thereby enhancing the trustworthiness of the output results.

IV. System Evaluation

In this section, we first explain the implementation of *h*BP-Fi along with experiment setup, then we conduct a thorough evaluation on *h*BP-Fi under various parameter settings.

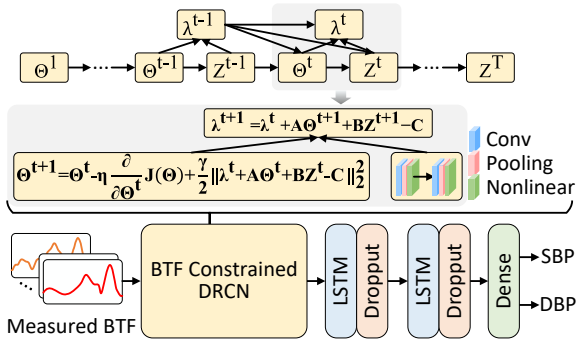

Fig. 9. BP estimator's pipeline with the BTF-constrained DRCN structure.

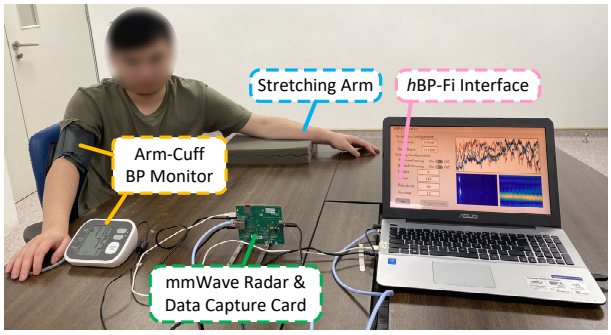

Fig. 10. Experiment setup with all devices exhibited.

A. Prototyping and Experiment Setup

a) Hardware and Software: *h*BP-Fi adopts an mmWave radar as the sensing front end for simultaneously monitoring varying pulse waveforms along the arm, and a laptop is used as the data processing back end. The adopted radar is a commercially available TI AWR1843BOOST mmWave radar [20]. It operates at 77 GHz, with 3 Tx antennas and 4 Rx antennas, and a bandwidth of up to 4 GHz. A TI DCA 1000EVM data capture adapter [40] is connected to the radar to acquire real-time data and stream them to the laptop. During data collection, the frame sampling rate is set to 200 frames/second. *h*BP-Fi's data processing pipeline is implemented in MATLAB R2019b and Python 3.8. The DL pipeline is built upon TensorFlow 2.2. We first processed the captured FMCW reflections as described in Sec. III-B2 to obtain pulse waveforms, then apply a sliding window of 512 samples shifted by 64 samples to infer BP.

b) Data Collection: We recruit 35 subjects (22 males and 13 females aged between 20 to 54) without known medical conditions related to our evaluation; this study is conducted with the approval of our institute's ethics committee. The experiment setup is shown in Fig. 10: by the standard validation procedure for BP monitoring [22], we ask the subjects to sit with their backs supported, legs uncrossed, and stretch his/her arm. The mmWave radar is placed in front of the subject with its FoV covering the whole arm area; it scans pulse waveforms along the arm while the subject maintains minimal body movements. The ground truth of BP is obtained using an FDA-approved arm-cuff BP monitor Omron 7127 [41], with the arm cuff held at heart level. This device only delivers ground truth BPs for training *h*BP-Fi; it is not part of *h*BP-Fi in practical usage. We particularly collect data at various clock times and temperatures to evaluate the system's robustness to these factors. As the relative angle and distance between the arm and radar can vary arbitrarily during actual use, we also study *h*BP-Fi's performance with varying radar placements. Overall, we collect approximately 252,000 heartbeat cycles.

c) Evaluation Methodology: To evaluate *h*BP-Fi, we use two widely adopted metrics, i.e., mean error $\mathrm{ME} = \sum_{i=1}^{n}(\tilde{\rho}_i - \rho_i)/n$ and standard deviation of mean error $\mathrm{STD} = \sqrt{\sum_{i=1}^{n}(\tilde{\rho}_i - \rho_i - ME)^2/n}$, where $\tilde{\rho}$ and ρ respectively denote the estimated and ground truth (true) BP values.

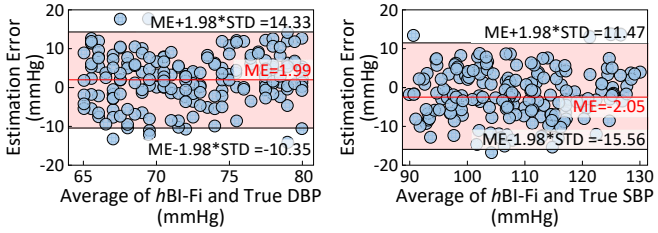

(a) DBP. (b) SBP.

Fig. 11. The overall performance of *h*BP-Fi.

B. System-Level Evaluation

1) Overall Performance: We first study *h*BP-Fi's ability in estimating BP, leveraging RF-sensed pulse waveforms. Results from the five-fold cross-validation experiment are illustrated in Fig. 11, which shows the Bland-Altman plots for the estimated SBP and DBP. More than 95% points are narrowly distributed within the limits of agreement, i.e., ME$\pm$1.98$\times$STD, suggesting that the estimated BP can be an alternative to the true BP. Overall, *h*BP-Fi achieves the ME of -2.05 mmHg and STD of 6.83 mmHg for estimating SBP and ME of 1.99 mmHg and STD of 6.30 mmHg for estimating DBP. Such decent performance confirms the effectiveness of *h*BP-Fi.

To further validate *h*BP-Fi, we compare the results of five-fold cross-validation experiment with the acceptable range regulated by the Association for the Advancement of Medical Instruments (AAMI) [22] and the requirement for the Britain Hypertension Society (BHS) standard [42] in Tables II and III, respectively. One may readily observe that *h*BP-Fi satisfies the recommended error boundary defined by the AAMI and achieves BHS Grade A for estimating DBP and SBP. It is worth noting that a recent proposal mmBP [16] claims to achieve slightly lower estimation errors. However, as mmBP takes a black-box DL model to "translate" single-site pulse measurements to BP readings in a brute-force manner, its lack of physiological basis makes one suspect a potential overfitting by testing on data already used for training. On the contrary, *h*BP-Fi is constructed upon a solid physiological basis and realized by an explainable DL model to achieve accurate BP estimation, so its performance firmly justifies an alternative to the FDA-approved cuff-based BP monitor.

TABLE II
COMPARING *h*BP-FI WITH AAMI STANDARD.

		ME (mmHg)	STD (mmHg)
*h*BP-Fi	SBP	-2.05	6.83
	DBP	1.99	6.30
AAMI	SBP and DBP	$\leqslant$5	$\leqslant$8

TABLE III
COMPARING *h*BP-FI WITH BHS STANDARD.

		Cumulative Error Percentage		
		$\leqslant$5 mmHg	$\leqslant$10 mmHg	$\leqslant$15 mmHg
*h*BP-Fi	SBP	61.50%	86.63%	97.65%
	DBP	62.57%	87.82%	98.93%
BHS	Grade A	60%	85%	95%
	Grade B	50%	75%	90%
	Grade C	40%	65%	85%

2) Impact of Environment Factors: We are interested in how *h*BP-Fi would perform in diverse real-world environments. Therefore, we group the dataset according to temperature and clock time. Data from one environment is used for testing, while data from the remaining environments is used for training; this leave-one-*environment*-out experiment ensures that the training and testing are mutually exclusive and that *h*BP-Fi is evaluated in an untrained environment. Fig. 12 shows the results with more than 95% of the points in the limits of agreements. Specifically, *h*BP-Fi achieves the ME of -2.95 mmHg and STD of 7.66 mmHg for estimating SBP and ME of 2.63 mmHg and STD of 6.50 mmHg for estimating DBP. The promising results confirm that *h*BP-Fi is capable of being an alternative solution for accurate BP monitoring and can successfully handle environment factor variations.

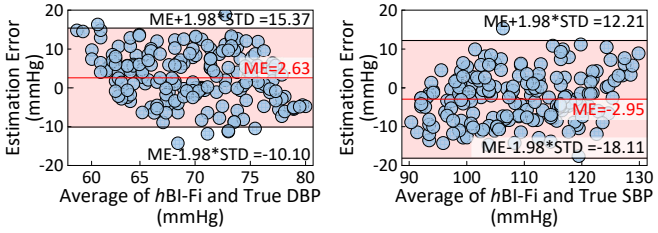

(a) DBP. (b) SBP

Fig. 12. Performance of *h*BP-Fi in leave-one-environment-out experiment.

3) Impact of Radar Placement: In real-world environments, the distance and angle between the subject's arm and the radar may be different. To understand whether the changes in radar placement affect system performance, we conduct experiments by asking the subjects to collect data with distance $d = \{30\text{ cm}, 50\text{ cm}, 70\text{ cm}, 90\text{ cm}\}$ and angle $\zeta = \{0°, 15°, 30°, 45°\}$. Table IV summarizes the ME and STD quantified by the above factors. Overall, the performance of *h*BP-Fi is stable as the angle changes. Besides, we notice that the SBP and DBP are negatively affected by the increasing sensing distance. Encouragingly, both SBP and DBP remain within the acceptable range regulated by the FDA protocol when the distance is within 90 cm. Since most people are fine with a measure distance within 90 cm, *h*BP-Fi has confirmed robustness in real-world adoption.

C. Micro-benchmark Evaluation

1) Effectiveness of Super-Resolution Beam Scan (SRBC): SRBC is critical to obtain fine-grained BTFs and further

TABLE IV
PERFORMANCE WITH DIFFERENT RADAR PLACEMENTS.

	ζ \ d	30 cm	50 cm	70 cm	90 cm
SBP	0°	-2.05±6.76	-2.04±6.72	-2.35±7.21	-3.47±7.12
	15°	-2.00±6.74	-2.03±6.77	-2.15±7.36	-3.46± 7.61
	30°	-2.02±6.81	-2.07±6.91	-2.48±7.11	-3.46±7.79
	45°	-2.06±6.92	-2.05±6.85	-2.10±7.20	-3.48±7.77
DBP	0°	1.99±6.31	2.03±6.82	2.68±7.47	4.33±7.22
	15°	2.07±6.30	2.04±6.51	2.69±6.63	3.34±7.30
	30°	2.09±6.35	2.09±6.53	2.68±6.78	3.29±7.72
	45°	2.03±6.34	2.06±7.72	2.69±7.28	3.36±7.87

obtain accurate BP. Therefore, we conduct an experiment to compare our SRBC scheme with a traditional beamforming scheme [36], leaving other system components intact. In the case of using the traditional beamforming scheme, pulse waves derived from particular angel bins [36] are treated as pulse waves at particular arm sites. Fig. 13 compares the estimation error for SBP and DBP using the two sensing schemes, where the points represent ME and the error bars indicate STD. Without using the SRBC scheme, the estimation error between system outputs and true BP achieves -5.72 ± 17.65 mmHg and 2.89 ± 14.01 mmHg for SBP and DBP, respectively. These are, however, reduced by our SRBC to -2.05 ± 6.83 mmHg and 1.99 ± 6.30 mmHg for SBP and DBP, respectively. These results indicate that, as we discussed in Sec. III-B1, the SRBC is effective and indeed yields more accurate BP estimates.

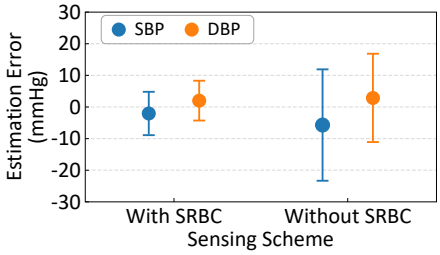

Fig. 13. Performance with different sensing schemes.

2) Resolution of Null Steering: The distribution of null points determines the resolution of null steering. More null points may result in too little variation between pulse waveforms, making it difficult to characterize hemodynamics. Fewer null points, on the other hand, would result in fewer pulse waveforms being captured along the arm, which could hinder BTF optimization. Without pulse signals from multiple arm locations, we infer the resolution of null steering by assessing the accuracy of BP measurements at different candidate distributions. We particularly collect data at intervals of 4°, 6°, 8°, 10°, and 12° between null points, all finer than the width of the main beam of 14°. Fig. 14 shows both MEs and STDs for SBP and DBP estimates; one may observe that i) MEs do not vary significantly from intervals 4° to 6°, while STD for SBP slightly decreases and the STD for DBP slightly increases, ii) MEs and STDs decrease noticeably after the interval reaches 8° and 10°, and iii) MEs and STDs become relatively saturated till the interval of 12°. Such results indicate that the resolution of our null steering approach is enhanced from 14° to 8°.

3) Explainability in DL: Despite the clarification of DL model's explainability in Sec. III-C, we further demonstrate the explainability in DL by showcasing how changes in the inputted BTFs are associated with variations in the estimated BP values, providing insights into the BP-estimating process. To achieve this, we employ *shapley additive explanations* (SHAP) [43] to present visual explainability of the impact of different features on BP measurement. Specifically, each BTF input is divided into 64 groups, where the mean of each group serves as a feature, and SHAP values are computed using SHAP gradient explainer. The top panel of Fig. 15

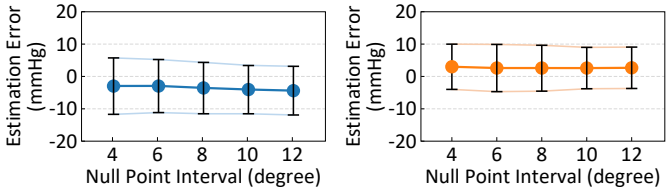

(a) Estimation error for SBP (b) Estimation error DBP

Fig. 14. Impact of null point intervals.

illustrates BTF features for two instances of SBP/DBP values from the same user: 110/74 and 103/72, while the bottom panel shows the corresponding SHAP values, where higher SHAP values indicate more significant contributions to BP variations. It can be observed that features #10 to #30 exhibit significant variations accompanied by higher SHAP values, while the remaining features show minimal changes with lower SHAP values. This direct association between the changes in BTF features and BP variations establishes a clear linkage, addressing the challenge of uncorrelated BP changes with BTF variations in the black-box DL setting. By assessing the consistency of BTF features with medical literature, such as prospective clinical trials and physiological mechanisms, users and clinicians can validate the BP results.

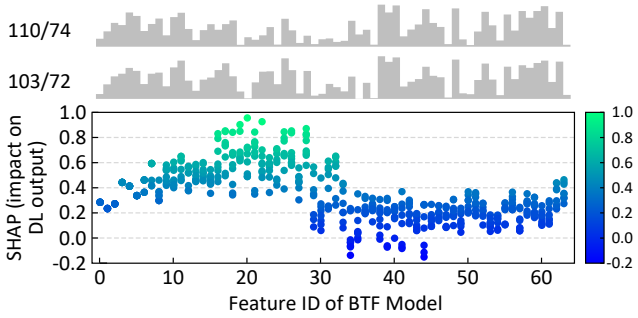

Fig. 15. The SHAP plot of features from BTF.

V. Conclusion

Contactless BP monitoring is a critical yet challenging problem in assessing health conditions, detecting potential diseases, and improving overall well-being. This paper serves as the first step towards such an ambition, driven by a sound physiological basis while leveraging commodity mmWave radar and explainable DL technologies. We implement *h*BP-Fi based on a novel proposition to infer accurate BP via BP-encoded hemodynamics of pulses transiting along arm arteries. Specifically, we thoroughly study the hemodynamics and introduce BTF that characterizes the underlying BP information in pulse waveforms. To obtain BTF via RF sensing, we develop a beam-steerable RF sensing that achieves super-resolution recovery of waveforms with a granularity finer than the minimum angular separation. Employing a carefully designed BTF-constrained pipeline, we equip *h*BP-Fi with an explainable DL that ensures accurate BP estimation and effective adaptation to various real-world environments. Via extensive experiments on 35 subjects, we demonstrate the promising performance of *h*BP-Fi in BP inference, hence confirming *h*BP-Fi's significant implications to various medical applications.

REFERENCES

[1] Centers for Disease Control and Prevention, "Facts About Hypertension," 2023. [Online]. Available: https://www.cdc.gov/bloodpressure/facts.htm

[2] M. J. Bloch, "Worldwide Prevalence of Hypertension Exceeds 1.3 Billion," *Journal of the American Society of Hypertension*, vol. 10, no. 10, pp. 753–754, 2016.

[3] F. Fan, Y. Gu, J. Shen, F. Dong, and Y. Chen, "FewShotBP: Towards Personalized Ubiquitous Continuous Blood Pressure Measurement," *Proc. of the ACM IMWUT*, vol. 7, no. 3, pp. 1–39, 2023.

[4] L. A. Geddes, M. Voelz, C. Combs, D. Reiner, and C. F. Babbs, "Characterization of the Oscillometric Method for Measuring Indirect Blood Pressure," *Annals of Biomedical Engineering*, vol. 10, no. 6, pp. 271–280, 1982.

[5] Y. Yoon, J. H. Cho, and G. Yoon, "Non-Constrained Blood Pressure Monitoring Using ECG and PPG for Personal Healthcare," *Journal of Medical Systems*, vol. 33, no. 4, pp. 261–266, 2009.

[6] Y. Cao, H. Chen, F. Li, and Y. Wang, "Crisp-BP: Continuous Wrist PPG-Based Blood Pressure Measurement," in *Proc. of the 27th ACM MobiCom*, 2021, pp. 378–391.

[7] Omron, "HeartGuide, Blood Pressure Anytime, Anywhere," 2023. [Online]. Available: https://omronhealthcare.com/products/heartguide-wearable-blood-pressure-monitor-bp8000m/

[8] N. Bui, N. Pham, J. J. Barnitz, Z. Zou, P. Nguyen, H. Truong, T. Kim, N. Farrow, A. Nguyen, J. Xiao, R. Deterding, T. Dinh, and T. Vu, "eBP: A Wearable System for Frequent and Comfortable Blood Pressure Monitoring From User's Ear," in *Proc. of the 25th ACM MobiCom*, 2019, pp. 1–17.

[9] C. Holz and E. J. Wang, "Glabella: Continuously Sensing Blood Pressure Behavior Using An Unobtrusive Wearable Device," *Proc. of the ACM IMWUT*, vol. 1, no. 3, pp. 1–23, 2017.

[10] K. Qian, C. Wu, F. Xiao, Y. Zheng, Y. Zhang, Z. Yang, and Y. Liu, "Acousticcardiogram: Monitoring Heartbeats Using Acoustic Signals on Smart Devices," in *Proc. of the IEEE INFOCOM*, 2018, pp. 1574–1582.

[11] A. Wang, J. E. Sunshine, and S. Gollakota, "Contactless Infant Monitoring Using White Noise," in *Proc. of the 25th ACM MobiCom*, 2019, pp. 1–16.

[12] C. Cai, R. Zheng, and J. Luo, "Ubiquitous Acoustic Sensing on Commodity Iot Devices: A Survey," *IEEE Communications Surveys & Tutorials*, vol. 24, no. 1, pp. 432–454, 2022.

[13] C. Cai, H. Pu, P. Wang, Z. Chen, and J. Luo, "We Hear Your Pace: Passive Acoustic Localization of Multiple Walking Persons," *Proc. of the ACM IMWUT*, vol. 5, no. 2, pp. 1–24, 2021.

[14] Z. Chen, T. Zheng, and J. Luo, "MoVi-Fi: Motion-robust Vital Signs Waveform Recovery via Deep Interpreted RF Sensing," in *Proc. of the 27th ACM MobiCom*, 2021, pp. 392–405.

[15] H. Shi, J. Pan, Z. Zheng, B. Wang, C. Shen, and Y. Guo, "Radar-Based Blood Pressure Estimation Using Multiple Features," in *Proc. of the IEEE IMBioC*, 2022, pp. 183–185.

[16] Z. Shi, T. Gu, Y. Zhang, and X. Zhang, "mmBP: Contact-Free Millimetre-Wave Radar Based Approach To Blood Pressure Measurement," in *Proc. of the 20th ACM SenSys*, 2022, pp. 1–14.

[17] X. Fan, Q. Ye, X. Yang, and S. D. Choudhury, "Robust Blood Pressure Estimation Using an RGB Camera," *Journal of Ambient Intelligence and Humanized Computing*, vol. 11, no. 11, pp. 4329–4336, 2020.

[18] M. P. Ebrahim, F. Heydari, K. Walker, K. Joe, J.-M. Redoute, and M. R. Yuce, "Systolic Blood Pressure Estimation Using Wearable Radar and Photoplethysmogram Signals," in *2019 IEEE International Conference on Systems, Man and Cybernetics*, 2019, pp. 3878–3882.

[19] D. Hughes, C. F. Babbs, L. Geddes, and J. Bourland, "Measurements of Young's Modulus of Elasticity of the Canine Aorta With Ultrasound," *Ultrasonic Imaging*, vol. 1, no. 4, pp. 356–367, 1979.

[20] Texas Instruments, "IWR1843BOOST," 2023. [Online]. Available: https://www.ti.com/tool/IWR1843BOOST

[21] J.-O. Hahn, A. T. Reisner, and H. H. Asada, "Estimation of Pulse Transit Time Using Two Diametric Blood Pressure Waveform Measurements," *Medical Engineering & Physics*, vol. 32, no. 7, pp. 753–759, 2010.

[22] G. S. Stergiou, B. Alpert, S. Mieke, R. Asmar, N. Atkins, S. Eckert, G. Frick, B. Friedman, T. Graßl, T. Ichikawa *et al.*, "A Universal Standard for the Validation of Blood Pressure Measuring Devices: Association for the Advancement of Medical Instrumentation/european Society of Hypertension/international Organization for Standardization (AAMI/ESH/ISO) Collaboration Statement," *Hypertension*, vol. 71, no. 3, pp. 368–374, 2018.

[23] J. Gravenstein, D. A. Paulus, J. Feldman, and G. McLaughlin, "Tissue Hypoxia Distal to a Penaz Finger Blood Pressure Cuff," *Journal of Clinical Monitoring*, vol. 1, pp. 120–125, 1985.

[24] E. J. Wang, J. Zhu, M. Jain, T.-J. Lee, E. Saba, L. Nachman, and S. N. Patel, "Seismo: Blood Pressure Monitoring Using Built-in Smartphone Accelerometer and Camera," in *Proc. of the ACM CHI*, 2018, pp. 1–9.

[25] A. Secerbegovic, J. Bergsland, P. S. Halvorsen, N. Suljanovic, A. Mujcic, and I. Balasingham, "Blood Pressure Estimation Using Video Plethysmography," in *proc. of the 13th IEEE ISBI*, 2016, pp. 461–464.

[26] M. Guo, H. Ni, and A. Q. Chen, "OfficeBP: Noninvasive Continuous Blood Pressure Monitoring Based on PPT in Office Environment," in *Proc. of the ACM UbiComp/ISWC*, 2020, pp. 29–32.

[27] D. Buxi, J.-M. Redouté, and M. R. Yuce, "Blood Pressure Estimation Using Pulse Transit Time From Bioimpedance and Continuous Wave Radar," *IEEE Transactions on Biomedical Engineering*, vol. 64, no. 4, pp. 917–927, 2016.

[28] Williamson Manufacturing Co Ltd, "Peristaltic Pumps: Introduction," 2023. [Online]. Available: https://www.wmcpumps.com/blog/peristaltic-pumps-introduction

[29] A. Díaz, C. Galli, M. Tringler, A. Ramírez, and E. I. Cabrera Fischer, "Reference Values of Pulse Wave Velocity in Healthy People From an Urban and Rural Argentinean Population," *International Journal of Hypertension*, vol. 2014, pp. 1–7, 2014.

[30] M. Sharma, K. Barbosa, V. Ho, D. Griggs, T. Ghirmai, S. K. Krishnan, T. K. Hsiai, J.-C. Chiao, and H. Cao, "Cuff-Less and Continuous Blood Pressure Monitoring: A Methodological Review," *Technologies*, vol. 5, no. 2, pp. 1–21, 2017.

[31] R. Fogliardi, M. Di Donfrancesco, and R. Burattini, "Comparison of Linear and Nonlinear Formulations of the Three-Element Windkessel Model," *American Journal of Physiology-Heart and Circulatory Physiology*, vol. 271, no. 6, pp. H2661–H2668, 1996.

[32] G. Zhang, J.-O. Hahn, and R. Mukkamala, "Tube-Load Model Parameter Estimation for Monitoring Arterial Hemodynamics," *Frontiers in Physiology*, vol. 2, p. 72, 2011.

[33] K. Han and S. Hong, "MIMO Differential Radar Using Null Point Beams for Vital Sign Detection in the Presence of Body Motions," in *Proc. of the 19th IEEE EuRAD*, 2022, pp. 177–180.

[34] M. R. R. Khan and V. Tuzlukov, "Null-Steering Beamforming for Cancellation of Co-channel Interference in CDMS Wireless Communication System," in *Proc. of the 4th IEEE ICSPCS*, 2010, pp. 1–5.

[35] J. Xiong, H. Hong, L. Xiao, and X. Zhu, "Chest and Abdominal Signals Separation Based on SIMO Radar With Difference Beamforming," *IEEE Microwave and Wireless Components Letters*, vol. 32, no. 3, pp. 218–221, 2022.

[36] S. Ahmed, J. Park, and S. H. Cho, "Effects of Receiver Beamforming for Vital Sign Measurements Using FMCW Radar at Various Distances and Angles," *Sensors*, vol. 22, no. 18, p. 6877, 2022.

[37] K. Zhang, W. Zuo, S. Gu, and L. Zhang, "Learning Deep CNN Denoiser Prior for Image Restoration," in *Proc. of the IEEE CVPR*, 2017, pp. 3929–3938.

[38] H. Shen, M. Jiang, J. Li, C. Zhou, Q. Yuan, and L. Zhang, "Coupling Model-and Data-driven Methods for Remote Sensing Image Restoration and Fusion: Improving physical interpretability," *IEEE Geoscience and Remote Sensing Magazine*, vol. 10, no. 2, pp. 231–249, 2022.

[39] S. Boyd, N. Parikh, E. Chu, B. Peleato, J. Eckstein *et al.*, "Distributed Optimization and Statistical Learning via the Alternating Direction Method of Multipliers," *Foundations and Trends® in Machine learning*, vol. 3, no. 1, pp. 1–122, 2011.

[40] Texas Instruments, "DCA1000EVM," 2023. [Online]. Available: https://www.ti.com/tool/DCA1000EVM

[41] Omron, "Automatic Blood Pressure Monitor HEM-7121," 2023. [Online]. Available: https://www.omronhealthcare-ap.com/sg/product/11-hem-7121

[42] E. O'Brien, J. Petrie, W. Littler, M. de Swiet, P. L. Padfield, D. G. Altman, M. Bland, A. Coats, and N. Atkins, "The British Hypertension Society Protocol for the Evaluation of Blood Pressure Measuring Devices," *Jhypertens*, vol. 11, no. Suppl 2, pp. S43–S62, 1993.

[43] S. M. Lundberg and S.-I. Lee, "A Unified Approach to Interpreting Model Predictions," *Advances in Neural Information Processing Systems*, vol. 30, pp. 1–10, 2017.